applied sciences

MDPI

Article

Practical Methodology for a Three-Dimensional-Printed Hybrid Desalination System

Ziomara De la Cruz-Barragán [1], Elier Sandoval-Sánchez [1], Jonathan Israel Hernández-Hernández [1], Margarita Miranda-Hernández [2,*] and Edgar Mendoza [1,*]

[1] Instituto de Ingeniería, Universidad Nacional Autónoma de México, Ciudad Universitaria, Circuito Exterior S/N, Coyoacán, Mexico City 04510, Mexico; zdelacruzb@iingen.unam.mx (Z.D.l.C.-B.); esandovals@iingen.unam.mx (E.S.-S.); jhernandezhe@iingen.unam.mx (J.I.H.-H.)

[2] Instituto de Energías Renovables, Universidad Nacional Autónoma de México, Priv. Xochicalco, Temixco 62580, Mexico

* Correspondence: mmh@ier.unam.mx (M.M.-H.); emendozab@iingen.unam.mx (E.M.); Tel.: +52-(55)-56-22-9730 (M.M.-H.); +52-(55)-56-23-3600 (ext. 8957) (E.M.)

Featured Application: The developed methodology enables the rapid fabrication of customized lab-scale reactors, optimizing their design and manufacturing. Beyond desalination, this approach is valuable in the early R&D stages for other electrochemical flow reactors, such as fuel cells, bio-batteries, microfluidic devices, and electrolyzers.

Abstract: In response to the growing demand for potable water, this study presents a practical methodology for designing and fabricating a hybrid desalination system that integrates reverse electrodialysis and electrodialysis using 3D-printing technology. The hybrid system combines the energy generation potential of RED with the salt removal capabilities of ED, reducing energy consumption. Customized reactors were designed to enhance flow distribution and ion exchange, with computational fluid dynamics simulations validating the hydrodynamic performance. The reactors were fabricated using 3D printing, allowing rapid, cost-effective production, with functional reactors constructed in under 24 h. The system achieved a 15% reduction in salt concentration within one hour, with a specific energy consumption of 0.1388 Wh/m^3 and a water recovery rate of 50%. These results demonstrate the functionality of the RED-ED hybrid system for achieving energy savings and performing water desalination. This methodology provides a scalable and replicable solution for water treatment applications, especially in regions with abundant salinity gradients and limited freshwater resources, while offering a multidisciplinary approach that integrates physicochemical and engineering principles for effective device development.

Keywords: 3D printing; electrochemical flow reactor; desalination; salinity gradient energy; electrodialysis; reverse electrodialysis; CFD modeling

Citation: De la Cruz-Barragán, Z.; Sandoval-Sánchez, E.; Hernández-Hernández, J.I.; Miranda-Hernández, M.; Mendoza, E. Practical Methodology for a Three-Dimensional-Printed Hybrid Desalination System. *Appl. Sci.* **2024**, *14*, 10905. https://doi.org/10.3390/app142310905

Academic Editor: Rocco Furferi

Received: 28 October 2024
Revised: 16 November 2024
Accepted: 21 November 2024
Published: 25 November 2024

1. Introduction

Desalination is an ancient and extensively studied process that separates or extracts salt from water, reducing salt content or producing fresh water [1,2]. Modern desalination technologies encompass both thermal and membrane processes, with electrodialysis (ED) being a notable example [3–5]. While essential for meeting the increasing demand for potable water, desalination processes have a significant environmental impact. Globally, approximately 142 million m^3 of brine is produced daily, posing a major environmental challenge [1]. Additionally, desalination is energy-intensive, with the global desalination capacity requiring over 850 million tons of oil annually, leading to the emission of 76 million tons of CO_2, contributing to climate change [6]. In recent years, there has been an increasing trend toward integrating renewable energy technologies into desalination processes [3,7]. This integration is driven by the desire to reduce greenhouse gas emissions, minimize

resource use, and mitigate excessive energy consumption, representing more than 50% of desalination process prices [3]. As the costs of these technologies continue to decrease, hybrid desalination systems are expected to become more economically viable, offering more sustainable and cost-effective long-term solutions.

One of the renewable energy sources that can synergize with desalination systems is osmotic energy, also known as salinity gradient energy (SGE) or blue energy. SGE is an innovative renewable energy technology that exploits the energy potential generated when two bodies of water with varying salt concentrations merge [8,9]. The concept was first introduced by Robert Pattle in 1954 [10], who showed that salinity differences can be converted into electrical energy using ion exchange membranes (IEMs). Since then, SGE has garnered significant research interest, with key technologies such as pressure-retarded osmosis, reverse electrodialysis (RED), and capacitive mixing emerging as the most promising approaches for efficiently capturing this energy source [11–14]. These technologies offer a sustainable and untapped avenue for renewable energy generation, particularly in coastal regions with abundant fresh and saltwater bodies.

RED and ED reactors are electrochemical flow reactors consisting of several internal compartments separated by alternating anion exchange membranes (AEMs) and cation exchange membranes (CEMs). At the ends of the cell, they feature an electrode system that includes an electrode rinse solution (ERS). However, while the RED reactor is a galvanic system that generates energy by harnessing the spontaneous movement of ions down their concentration gradient, the ED system requires an external energy source to drive the desalination process by forcing ions to migrate against the chemical potential. Figure 1a illustrates a RED unit cell, where a high-concentration saline solution (H) and a low-concentration solution (L) are separated by IEMs, creating a chemical potential difference. This gradient drives the diffusion of anions (Cl^-) through AEMs and cations (Na^+) through CEMs, generating an ionic current. Electrodes at the ends of the cell convert this ionic current into electrical energy through redox reactions. Figure 1b shows an ED reactor. In this case, a saline feed solution (F) flows through the compartments, and an external power source polarizes the electrodes. The electric field causes anions and cations to migrate toward the anode and cathode, respectively. The selective membranes reduce the salt concentration in one compartment, producing desalinated water (D), while the adjacent compartment accumulates the removed salts, resulting in a brine solution (B).

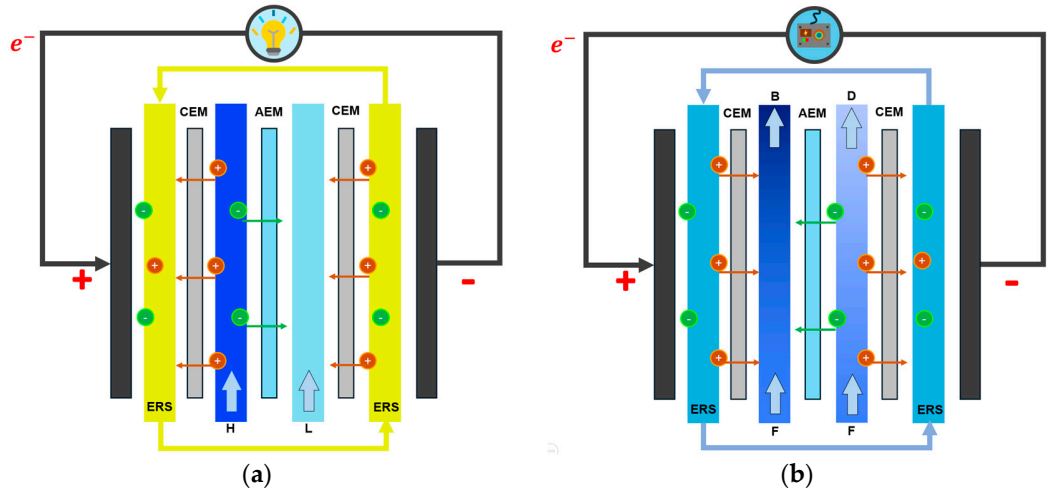

Figure 1. RED and ED cells: (**a**) diagram of a RED unit cell; (**b**) diagram of an ED unit cell.

Several hybrid desalination systems combining RED and ED have been developed, with both external (RED-ED) and internal configurations (RED/ED). Externally integrated systems, like those proposed by Wang et al. (2017) and Luo et al. (2017), involve independent RED and ED reactors, where RED acts as a pre-desalination step or an energy donor for the ED process [15,16]. Their findings demonstrated the system's feasibility, achieving

desalinated water conductivity as low as 72 µS/cm, suitable for human consumption [16]. While these systems are feasible, they suffer from low energy efficiency due to converting chemical and electrical energy. Internally integrated systems, such as the one introduced by Chen et al. (2015), couple RED and ED within a single reactor, using the salinity gradient energy from seawater and brine to drive the ED process directly. This system produced 48.3 L of fresh water (~420 mg/L) daily, consuming 229.4 L of brine and 132.8 L of seawater [17]. In an internally integrated hybrid system, the desalination process is directly powered by ion flow, minimizing energy losses from conversion processes. Furthermore, RED/ED systems only require a single pair of electrodes, whereas external integrations use two pairs. However, the performance of internally integrated RED/ED reactors is influenced by numerous factors, such as electrolyte concentration, the number of unit cells, and the thickness of the solution compartments [18]. Hybrid RED-ED systems can utilize the residual brine from ED, a byproduct of desalination, to generate energy through RED. Furthermore, the modularity of RED and ED reactors facilitates the system scale-up. The study of desalination systems and devices, such as RED and ED, at the laboratory level is essential for advancing their development. Three-dimensional printing enables the creation of customized devices that optimize the design of these reactors. This technology not only facilitates research but also makes the development of tailored prototypes more accessible, bridging the gap between experimental research and the practical implementation of desalination solutions.

Since its inception in the 1980s, 3D printing, also known as additive manufacturing, has gained widespread popularity across various industries and research fields due to its remarkable versatility in producing an endless array of three-dimensional models using innovative materials. While the application of 3D printing in the fabrication of electrochemical reactors is still in its early developmental phase [19], a growing body of research has already explored its potential in areas such as energy generation [20], desalination [21], batteries [22], biosensors [23], electrode manufacturing [24], and electrochemical sensing devices [25]. Additive manufacturing presents significant advantages for the design and development of RED/ED systems, as it enables the fabrication of intricate geometries that improve the hydrodynamic performance and overall efficiency of the system [26]. Despite these advancements, most studies have focused on 3D printing individual components of reactors. To date, a comprehensive methodology that integrates the design, fabrication, and electrochemical characterization of a laboratory-scale RED-ED desalination system has not been reported. Addressing the multidisciplinary interactions between processes, materials, and structural components is fundamental to driving the ongoing development and improvement of these systems.

The use of 3D printing can significantly speed up the development of RED/ED reactors, particularly during the early stages, by enabling the rapid fabrication of laboratory-scale prototypes tailored to precise design and geometry specifications. Additionally, it allows for easy adjustments to various parameters, facilitating future scalability for full-scale applications or industrial use. In-house production of these reactors not only offers the flexibility to customize designs to meet specific requirements but also helps reduce both costs and production times. This article introduces a practical methodology for the development of a hybrid desalination system combining RED and ED, designed to be replicable in other laboratories. It covers the entire process, including the design of 3D-printed reactor components, the fabrication process using 3D printing, CFD simulations, slicer configuration, printing recommendations, and the electrochemical characterization of the system for performance validation. The efficacy of the RED and ED devices was evaluated separately, and the desalination performance of the hybrid RED-ED system was demonstrated. Additionally, a repository is provided containing the 3D design files for the reactor components. The results of this study show that a functional hybrid RED-ED desalination system can be developed more efficiently, at a lower cost, and in less time, offering a scalable and cost-effective solution for water desalination.

2. Materials and Methods

2.1. Reactor Geometry

Electrochemical flow reactors have numerous applications, allowing for a wide range of geometries and configurations [19]. The choice of reactor geometry will depend on its ability to promote the hydrodynamic phenomena best suited for each specific application. Cervantes-Alcalá and Miranda-Hernández (2018) highlighted the importance of optimizing geometry in redox flow batteries to enhance flow uniformity, outperforming conventional square reactors [27]. Conventional RFB reactors are designed with two compartments for electrolyte flow, while RED and ED cells require three compartments for freshwater, saltwater, and an ERS. Based on the optimizations and geometry proposed by Cervantes-Alcalá and Miranda-Hernández (2018), two geometries were designed, incorporating two different manifolds adapted to meet the specific needs of RED and ED reactors. These modifications allow for the implementation of multiple inlets and outlets, ensuring efficient fluid distribution within the system.

2.2. Computational Fluid Dynamics Study

Since the solutions in flow reactors are in a liquid state, it is essential to study the hydrodynamic phenomena occurring inside them. These phenomena such as mass transport and distribution, pressure profiles, and the presence of stagnation zones play a crucial role in the reactor's performance, as they directly influence the ion exchange processes. Different hydrodynamic processes and their relationship with the reaction mechanisms of the devices are deeply studied [25–30]. Hydrodynamic phenomena in RED and ED systems can be addressed in different ways, from the study of particle behavior to the analysis of flow in specific areas of the system. The equations that describe these phenomena are complex, and although three-dimensional simulations provide a more accurate representation, their implementation requires many computational resources. In this study, a more efficient approach was chosen using two-dimensional simulations that allowed for evaluating the velocity profile in the contour of the proposed geometries, to analyze the flow distribution inside the reactor. Computational fluid dynamics (CFD) simulations were employed to evaluate the proposed reactor geometries. Eight different flow velocities were tested to determine the most efficient pump flow rate. This study focuses on the physical limitations of pump velocities achievable for the proposed RED-ED reactor dimensions.

The simulations were performed using COMSOL Multiphysics 5.3 software, under the license provided by the Engineering Institute of UNAM. One of the most widely used mathematical models for hydrodynamic studies is the Navier–Stokes model, which consists of a set of partial differential equations that comprise the fluid motion equations for each coordinate component [31]; the momentum transport equation, Equation (1), and the continuity equation, Equation (2), of the Navier–Stokes model for an incompressible Newtonian fluid at steady state, were used.

$$\rho(u\cdot\nabla)u = \nabla\cdot\left[-p\tilde{\tau} + \mu\left(\nabla u + (\nabla u)^T\right)\right] + F + \rho g, \quad (1)$$

$$\rho\nabla\cdot(u) = 0, \quad (2)$$

where ∇ is the fluid density, u is the velocity, p is the pressure, $\tilde{\tau}$ is the identity matrix, μ is the viscosity, T is the temperature, and F represents the external forces.

2.3. CAD Design

Based on the studied geometries for the ED and RED reactors, the components of the devices were designed, including gaskets, flow distributors (FDs), end plates, and compression plates. The arrangement of the gaskets and FDs forms the compartments for the saline solutions and electrode rinse solutions. The gaskets primarily function as seals to prevent external leaks and cross-contamination. Material choice for the gaskets is crucial, as it impacts the reliability of the seal and fluid distribution. For optimal performance,

materials with an appropriate Shore hardness are selected to ensure flexibility and resilience; a material that is too rigid may not seal properly, whereas a material that is overly soft or thin could deform or tear under pressure, compromising the seal. Therefore, choosing an adequate Shore hardness is essential to balance flexibility and strength according to the specific requirements of the gasket component. The FD, designed to ensure uniform fluid distribution within the compartments, is constructed to provide structural stability while minimizing stagnation zones. The material for the FD must withstand constant fluid flow without excessive deformation, which could impede fluid distribution and lead to pressure imbalances within the reactor.

End plates and compression plates, which house fluid inlets and outlets and secure the stack alignment, require materials that can tolerate high-compression forces. Excessively thick materials in these components may increase mechanical resistance and compromise the overall pressure distribution. The compression plates apply even pressure throughout the reactor stack, preventing leaks and maintaining alignment. The 3D design of the reactor components was created using the open-source CAD platform Fusion 360 (Autodesk). Figure 2a,b show the design of the gaskets and the meshed FD, with a geometric area of 30 cm^2 and a thickness of 1 mm. Figure 3 presents a CAD model of the reactor, including all previously described components. The use of a 3D CAD model in the design process enables precise visualization of component assembly, helping identify alignment or fitting issues early, which allows for necessary adjustments before manufacturing and ultimately saves time and resources.

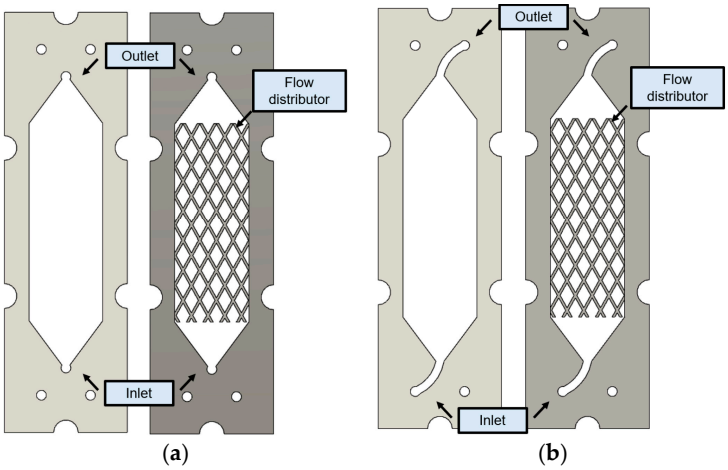

Figure 2. Design gaskets and FD: (**a**) design of gaskets and FD for the ERS; (**b**) design of gaskets and FD for saline solutions.

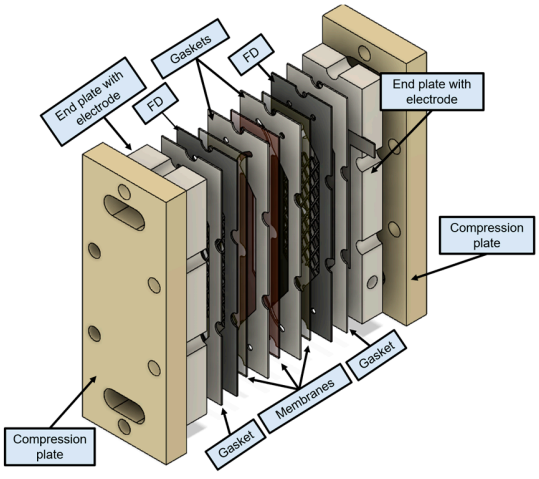

Figure 3. CAD model of the assembled reactor.

2.4. Three-Dimensional Printing

For the manufacturing of the reactor components, the CAD design was converted into a coordinate file format for the printer, known as Standard Triangle Language (.STL). For the end plates and FD, the material must have high mechanical strength, as the parts will be subjected to compression and high chemical resistance to withstand varying pH levels. The end plates and FD were produced using the Fortus® 450mc 3D production system (Stratasys Ltd., Edina, MN, USA). Acrylonitrile Styrene Acrylate (ASA), an engineering plastic (Stratasys Ltd.), was selected for its high mechanical strength and chemical resistance. The ASA material is designed to withstand substantial pressures, with a compression limit of 75.4 MPa in the XZ orientation and 188 MPa in the ZX orientation, according to the manufacturer's specifications. Assembly of the reactors is performed using a torque of 6 Nm to ensure a secure fit without over-compressing the components. Excessive compression is not recommended, as it may lead to the deformation of internal parts, rupture of membranes, or even constriction of the channels supplying the reactor. Although the material can tolerate significant pressure, maintaining a controlled pressure level is essential to preserve the integrity and functionality of the reactor structure, thus avoiding potential issues associated with high-pressure desalination processes.

The printing process was configured using an Insight slicer, which converts STL files into CMB files (a format containing the print path and settings for 3D printers). Both the end plates and FD were printed solid (100% infill) to prevent electrolyte permeation, using a nozzle with a layer height of 0.1778 mm for high-dimensional precision. For the gaskets, a flexible yet durable material is required. Thermoplastic polyurethane (TPU) is a good choice for printing gaskets due to its combination of elasticity, abrasion resistance, and chemical durability. Various TPU formulations are determined by their Shore hardness, which affects the material's rigidity and flexibility. In 3D printing, a lower Shore hardness indicates more flexibility, while a higher Shore hardness results in greater rigidity. TPU 95A was selected, and 1 mm thick gaskets were printed using an Ultimaker 2 Extended+ printer (Ultimaker, Utrecht, The Netherlands). The process was configured in a Cura slicer, utilizing a nozzle with a 0.6 mm layer height. The fabrication of two reactors (RED and ED) took a total of 20 h and 50 min, using a material volume of 606.97 cm^3. The total printing cost for both reactors, including the FD, gaskets, and end plates, was $232.46. Figure 4 shows the 3D-printed components used in the reactor assembly. In Figure 4a, a gasket printed in TPU 95A and an FD printed in ASA are displayed; Figure 4b shows the reactor assembled.

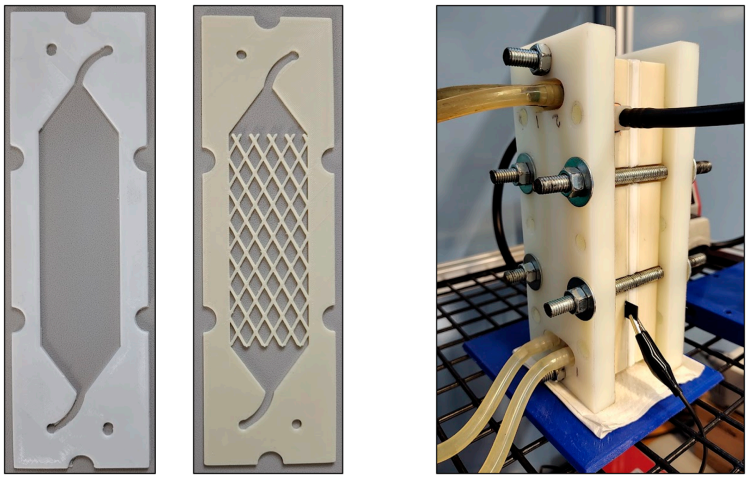

(**a**) (**b**)

Figure 4. Three-dimensional-printed components used in the reactor fabrication: (**a**) gasket printed in TPU 95A and FP printed in ASA; (**b**) assembled reactor.

2.5. Additional Materials

The compression plates were manufactured using a CNC milling machine with 17 mm thick Nylamid, ensuring high mechanical strength. Titanium plates coated with iridium and ruthenium (Magneto Special Anodes BV, Schiedam, The Netherlands) were used as electrodes, featuring a geometric area of 3×10 cm^2. These dimensionally stable electrodes were designed in a rectangular shape to fit the reactor's new geometry and include a side extrusion to facilitate contact between the plates. Ion-exchange polymer membranes (AEM and CEM Type 10) (FUJIFILM Manufacturing Europe BV, Tilburg, The Netherlands) were also used in the assembly; the technical specifications of the membranes used are shown in Table 1. Two peristaltic pumps with dual heads (model 323S) were used for handling the saline solutions in both the RED and ED processes, while two additional peristaltic pumps (model 120U/DV) were employed to recirculate the ERS in each reactor (WATSON-MARLOW, S de RL de CV, Nuevo Leon, Mexico). For the solutions, high-purity NaCl, potassium ferrocyanide ($K_4[Fe(CN)_6]\cdot 3H_2O$), and potassium ferricyanide ($K_3[Fe(CN)_6]$) were obtained from Sigma-Aldrich (St. Louis, MS, USA). All solutions were prepared with distilled water. A multimeter (SDM3055 SIGLENT Technologies) and a power supply (SPD3303X SIGLENT Technologies, Solon, OH, USA) were also used during the experiments.

Table 1. Main features of Fujifilm Type 10 membranes.

Specifications	AEM	CEM
Thickness dry (μm)	125	135
Electrical Resistance [1]	1.7	2.0
Perm selectivity [2]	95	99
IE Capacity [3]	1.8	1.5
Water permeation [4]	6.5	6.5
Burst strength [5]	2.8	2.8
pH stability	pH 1–13	pH 1–13
Temp stability [6]	60	60

[1] Electrical resistance measured Ω cm^2 at 2 M NaCl; [2] NaCl permselectivity measured at 0.05–0.5 M KCl; [3] ion exchange capacity (meq/g); [4] water permeation (ml/bar·m^2·h); [5] burst strength (kg/cm^2); [6] temperature (°C).

2.6. Fundamental Equations of the RED Process

The performance of the RED reactor is characterized through theoretical equations that estimate the potential difference across the membranes, the power output of the cell, and the contribution of resistance from various reactor components, among other aspects. Cipollina and Micale [8] indicate that the membrane potential difference (E_{IEM}) can be represented by a modified form of the Nernst equation, as detailed in Equation (3):

$$E_{IEM} = \alpha_{IEM} \frac{RT}{zF} ln \left(\frac{\gamma_c \times C_c}{\gamma_d \times C_d} \right) \text{ (V)}, \quad (3)$$

where α_{IEM} represents the membrane selectivity (%), R denotes the ideal gas constant (8.314 J/mol·K), T is the absolute temperature in Kelvin, z is the ion valence in solution, F stands for the Faraday constant, and γ_c, γ_d, C_c, and C_d refer to the activity coefficients and concentrations of the concentrated and diluted solutions (mol/L), respectively.

The electrical potential of a RED cell (E_{cell}) can be defined by the sum of the potentials from each membrane (E_{AEM} and E_{CEM}) and the number of repeated unit cells (N) present in the system, as shown in Equation (4). The resistance of a RED unit cell (R_{cell}) is calculated based on the resistances of the membranes (R_{AEM} and R_{CEM}) along with the resistance generated in the water compartments of the stack (R_c and R_d), as illustrated in Equation (5). The electric current (I) is determined using Equation (6), where R_{ext} represents the external resistance applied [8].

$$E_{cell} = N \times (E_{AEM} + E_{CEM}) \text{ (V)}, \quad (4)$$

$$R_{cell} = R_{AEM} + R_{CEM} + R_c + R_d \ (\Omega), \tag{5}$$

$$I = \frac{E_{cell}}{R_{cell} + R_{ext}} \ (\mathrm{A}), \tag{6}$$

The maximum power (P_{max}) generated by the RED reactor was calculated using Equation (7). To evaluate the power and current relative to the active membrane area (A_{mem}), the power density (P_d) and current density (J) were computed using Equations (8) and (9):

$$P_{max} = \frac{{E_{cell}}^2}{4R_{cell}} \ (\mathrm{W}), \tag{7}$$

$$P_d = \frac{P}{A_{mem}} \ \left(\frac{\mathrm{W}}{\mathrm{m}^2}\right), \tag{8}$$

$$J = \frac{I}{A_{mem}} \ \left(\frac{\mathrm{A}}{\mathrm{m}^2}\right). \tag{9}$$

2.7. Desalination Evaluation Parameters

In any desalination technique, it is necessary to evaluate certain key parameters that determine the efficiency and feasibility of the process. One of the most important reference parameters is the specific energy consumption (*SEC*), which relates to the amount of energy required to produce a specific volume of desalinated water. This parameter is crucial for comparing the energy efficiency across different desalination technologies. It was evaluated following the methodology proposed by Patel et al [32] using Equation (10):

$$SEC = \frac{(N\ V_c + V_{el})\bar{\mathrm{I}}A_{mem}}{N\ Q_d} \left(\frac{\mathrm{kWh}}{\mathrm{m}^3}\right), \tag{10}$$

where V_c represents the voltage per unit cell, V_{el} is the redox reaction potential at the electrodes, $\bar{I}$ denotes the average current density within a unit cell, and Q_d refers to the flow rate of desalinated water per unit cell.

Water recovery (*WR*) is used to quantify the ratio between the volume of produced water and the volume of feed water supplied [32]. It is evaluated using Equation (11), where Q_f represents the volumetric flow rate of the feed solution [33].

$$WR = \frac{Q_d}{Q_d + Q_f} \times 100 \ (\%). \tag{11}$$

The salt removal percentage (*SR*) is calculated as shown in Equation (12), where σ_d corresponds to the conductivity of the desalinated water, and σ_f refers to the conductivity of the feed water [31,32]. This percentage is determined based on conductivity values measured in mS/cm.

$$SR = \left(1 - \frac{\sigma_d}{\sigma_f}\right) \times 100 \ (\%) \ . \tag{12}$$

3. Results

3.1. CFD Simulations

Two-dimensional simulations of velocity profiles were carried out for the proposed geometries across a range of flow rates, as detailed in Table 2. These simulations evaluated different initial flow rates, considering the operational limits of the pump. The goal was to determine the optimal range of velocities that the pump could sustain under realistic operating conditions, ensuring effective performance while minimizing potential flow limitations. These results provide valuable insights into the hydrodynamic behavior of the system, helping to refine the design parameters for improved reactor efficiency.

Table 2. Velocity conditions for the evaluation of the proposed geometries.

Simulation	Flow Rate (mL/min)	Flow Velocity (m/s)
(a)	10	0.023
(b)	20	0.047
(c)	30	0.07
(d)	40	0.094
(e)	50	0.117
(f)	60	0.141
(g)	70	0.165
(h)	80	0.188

The following boundary conditions were set for modeling the geometries:

- 2D simulation;
- The fluid used in the simulation was pure water at 20 °C;
- Single-phase flow;
- Laminar flow;
- Steady-state condition;
- Incompressible fluid;
- Isotropic physical properties;
- No-slip condition at the walls;
- Outlet pressure set to 1 atm;
- Gravitational effects included;
- Hydrostatic pressure compensation condition applied.

Figure 5 shows the velocity profile simulations for the first geometry (geometry 1) at different initial flow rates. In Figure 5a, with a flow rate of 10 mL/min, the flow is evenly distributed throughout the reactor. However, as the flow rate increases from 20 mL/min to 80 mL/min (Figure 5b–h), the uniformity of the flow diminishes. Higher velocities, such as those in Figure 5b (20 mL/min) and Figure 5c (30 mL/min), lead to areas of higher speed near the inlet and outlet, with slower regions forming in the center of the reactor. This pattern becomes more pronounced at flow rates of 40 mL/min to 80 mL/min, where irregular flow patterns are shown. The highest velocities consistently appear at the inlet and outlet, which can result in reduced mass and ion transfer efficiency. These findings suggest that while geometry 1 performs well at lower flow rates, its efficiency decreases as flow rates increase, highlighting the need to consider these factors in the design and operation of electrochemical reactors.

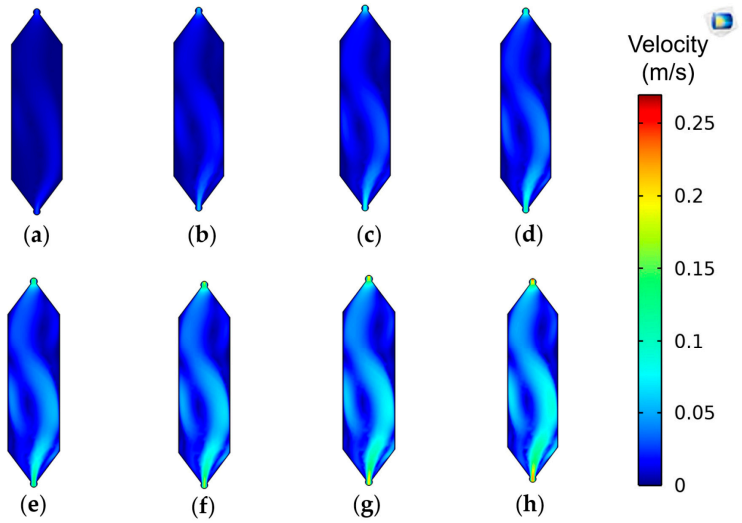

Figure 5. Velocity profile simulations of geometry 1 at different initial flow rates: (**a**) 10 mL/min, (**b**) 20 mL/min, (**c**) 30 mL/min, (**d**) 40 mL/min, (**e**) 50 mL/min, (**f**) 60 mL/min, (**g**) 70 mL/min, and (**h**) 80 mL/min.

Figure 6 presents the velocity profile simulations for the second geometry (geometry 2) at several initial flow rates. This geometry has distinctive curved inlets and outlets, specifically designed to provide greater fluid inlet flexibility. The flow appears relatively uniform at a low flow rate of 10 mL/min (Figure 6a), with the highest velocities concentrated near the curved inlets and outlets. As the flow rate increases (Figure 6b–h), the uniformity of the flow is reduced. Starting from 20 mL/min (Figure 6b) and 30 mL/min (Figure 6c), higher velocity zones begin to form near the inlets and outlets, while slower regions develop in the reactor's center. This pattern intensifies at higher flow rates, as seen in Figure 6d–h, where irregular flow patterns emerge. In all cases, the highest velocities are observed at the inlets and outlets, as expected from the design. However, as flow rates increase, the flow distribution becomes less uniform, potentially impacting mass and charge transfer within the reactor.

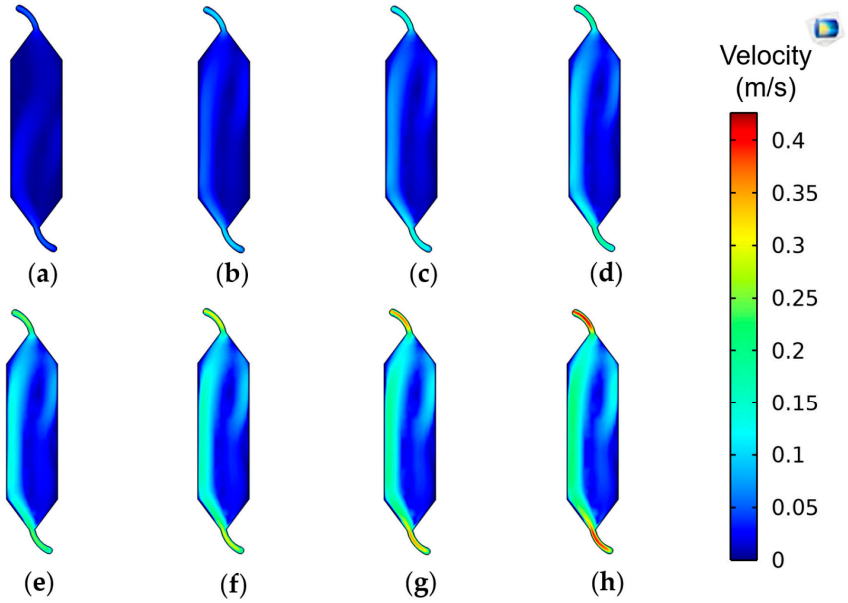

Figure 6. Velocity profile simulations of geometry 2 at different initial flow rates: (**a**) 10 mL/min, (**b**) 20 mL/min, (**c**) 30 mL/min, (**d**) 40 mL/min, (**e**) 50 mL/min, (**f**) 60 mL/min, (**g**) 70 mL/min, and (**h**) 80 mL/min.

The CFD simulations indicated distinct flow behaviors for the two geometries evaluated. Geometry 1 exhibited a more uniform flow distribution at lower velocities, and as the flow rate increased, stagnation zones were reduced. However, geometry 1 consistently reached lower velocities compared to geometry 2. In contrast, geometry 2 achieved higher flow velocities, though with reduced flow homogeneity. The choice of geometry should be made based on the specific application needs, whether prioritizing flow uniformity or achieving higher flow velocities. Geometry 1 was selected for the ERS compartments, where the high flow velocity is not crucial. On the other hand, geometry 2 was chosen for the saline solutions, as its higher flow velocities enhance ionic exchange across the membranes, promoting better mass transfer and more efficient ion transport.

3.2. RED Reactor Characterization

The RED reactor developed in this study was characterized using a unit cell, with a low-concentration solution of 3 g/L NaCl and a high-concentration solution of 35 g/L NaCl, simulating river water and seawater, respectively. Additionally, an ERS composed of 0.1 M $K_4[Fe(CN)_6]\cdot 3H_2O$, 0.1 M $K_3[Fe(CN)_6]$, and 0.3 M NaCl was utilized, with a total volume of 80 mL. For the NaCl solutions, a control volume of 500 mL was employed. The RED reactor's performance was evaluated at different flow rates of 20, 30, 40, 50, and 60 mL/min to assess the influence of hydrodynamic conditions on energy generation.

During the characterization, the open-circuit potential (OCP) and electric current were measured across a series of variable external resistances, ranging from 0 to 900 ohms, to determine the electrical behavior of the reactor. From these measurements, the power density was calculated to evaluate the reactor's capacity to generate energy under different operating conditions. This characterization aimed to determine the optimal operating conditions for energy production.

The results summarized in Table 3 provide a comparison between the experimental measurements and the theoretical predictions. The observed data indicate that the experimental results are consistent with the theoretical model, demonstrating the functionality of the developed RED reactor. Additionally, Figure 7 shows the effect of varying flow rates on the reactor's energy generation. As the flow rate increased, the power density improved, enhancing energy output due to better ionic exchange across the membranes. The highest energy generation was achieved at a flow rate of 60 mL/min, consistent with CFD simulations, which demonstrated that increasing flow velocity is an alternative to enhance energy production. Greater energy production could contribute to improved efficiency in the desalination process.

Table 3. Comparison between theoretical model and experimental results of RED reactor performance.

Evaluation	OCP (V)	J (A/m^2)	P_d (W/m^2)
Theoretical model	0.100	3.40	0.085
Experimental result	0.092	1.76	0.077

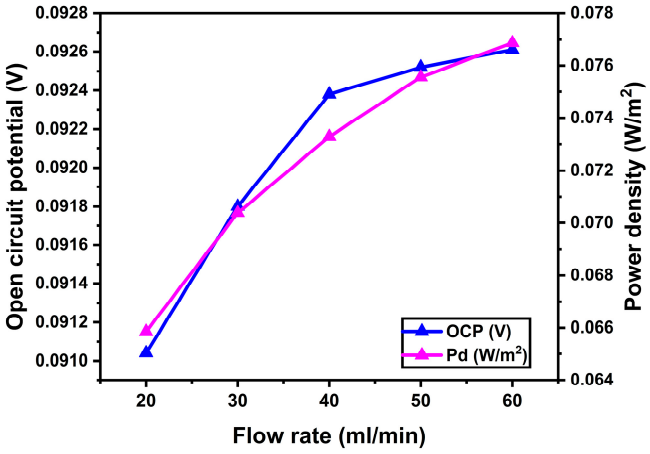

Figure 7. Effect of flow rate on open-circuit potential and power density in RED characterization.

3.3. ED Reactor Characterization

The efficiency of the constructed ED reactor was evaluated through desalination experiments using a NaCl solution of 10 g/L initial concentration, with a total volume of 1 L. This concentration represents typical brackish water conditions (1–10 g/L). Desalination of brackish water is of great interest for agricultural and domestic applications, where moderate salinity levels need to be reduced in an energy-efficient manner. An ERS consisting of 0.2 M NaCl was prepared to ensure consistent conductivity around the electrodes, facilitating proper electrochemical performance throughout the experiment. The experimental setup included the use of a unit cell to characterize the ED system. The ED reactor was paired with a power source that applied a constant theoretical potential of 0.1 V, equivalent to the electrical potential of a RED unit cell. This setup aimed to simulate conditions similar to a hybrid ED-RED system, with the specific purpose of evaluating the minimum desalination capability of the ED reactor. The applied voltage provided the necessary driving force for ion migration across the membranes, ensuring effective desalination during the process.

Higher flow rates improve desalination efficiency by reducing concentration polarization near the membrane surfaces, thereby enhancing ion transport across the compartments. Studies, including those by [34,35], demonstrate that increased flow rates decrease the thickness of the boundary layer, reducing resistance to ion migration and preventing ion buildup that otherwise hinders desalination. This effect allows for more efficient desalination, especially at higher initial salt concentrations. Desalination experiments were conducted over 60 min, with electrical conductivity measurements taken every 10 min to monitor the progression of salinity changes in both the desalinated and brine compartments. The initial conductivity in all reservoirs was set at 16.6 mS/cm. The results are illustrated in Figure 8, which depicts the variation in conductivity observed during the experiments conducted at different flow rates, ranging from 20 to 80 mL/min. The desalinated water compartment showed a consistent decline in conductivity over time, while the brine compartment experienced a corresponding increase. These trends demonstrate the direct impact of flow rate on the efficiency of ion transport between compartments.

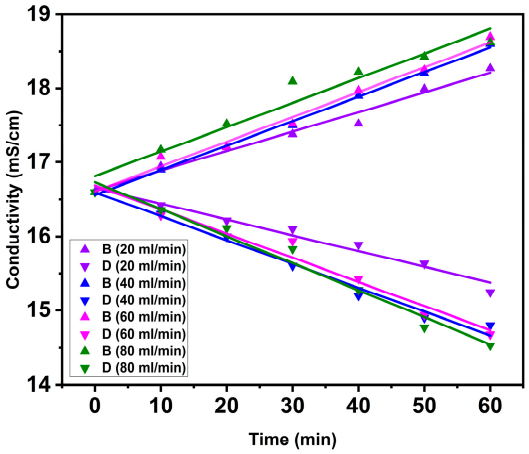

Figure 8. Conductivity variation during ED desalination at different flow rates.

The experimental data indicate that increasing the flow rate enhances the efficiency of the desalination process. Specifically, at the highest tested flow rate of 80 mL/min, the conductivity in the desalinated compartment decreased to a minimum of 14.53 mS/cm, corresponding to a salt removal efficiency of 12.46% over the one-hour experimental duration, as summarized in Table 4. These results demonstrate a positive correlation between flow rate and desalination efficiency, underscoring the importance of optimizing flow parameters to maximize ion removal and improve the overall effectiveness of the ED system.

Table 4. Salt removal efficiency at different flow rates.

Flow Rate (mL/min)	Salt Removal (%)
20	8.13
40	10.84
60	11.56
80	12.46

3.4. Performance of the Hybrid RED-ED System

The hybrid system was assembled using a single RED unit cell and a single ED unit cell, which were connected exclusively through an electrical circuit, with no fluid exchange between the units. The solutions used in each reactor were described in Sections 3.2 and 3.3; the RED unit used two solutions of different concentrations (H and L), while the ED unit used a saline feed solution for desalination. In this configuration, the RED unit generated the electrical energy required to power the ED reactor for desalination.

The RED reactor was tested in batch and continuous modes to determine whether the mode of operation influenced the energy supply to the ED reactor and, consequently, the desalination performance. In the batch mode, the salinity gradient in the RED reactor can decrease over time due to recirculation, which may reduce the energy available to drive the ED process. By comparing this setup with continuous mode operation in the RED reactor, where the salinity gradient is maintained more consistently, the experiment sought to understand if maintaining continuous operation in RED would be more favorable for consistent desalination in ED.

The ED reactor was operated in batch mode, with both the desalinated and brine solutions being recirculated. The recirculation aimed to increase desalination efficiency by enhancing the contact time between the feed solution and the membranes, thus promoting higher ion removal rates. Figure 9 illustrates the hybrid setup: Figure 9a shows a schematic of the system, highlighting the electrical connection and the independence of fluid circuits in each reactor, while Figure 9b displays a photograph of the complete experimental setup.

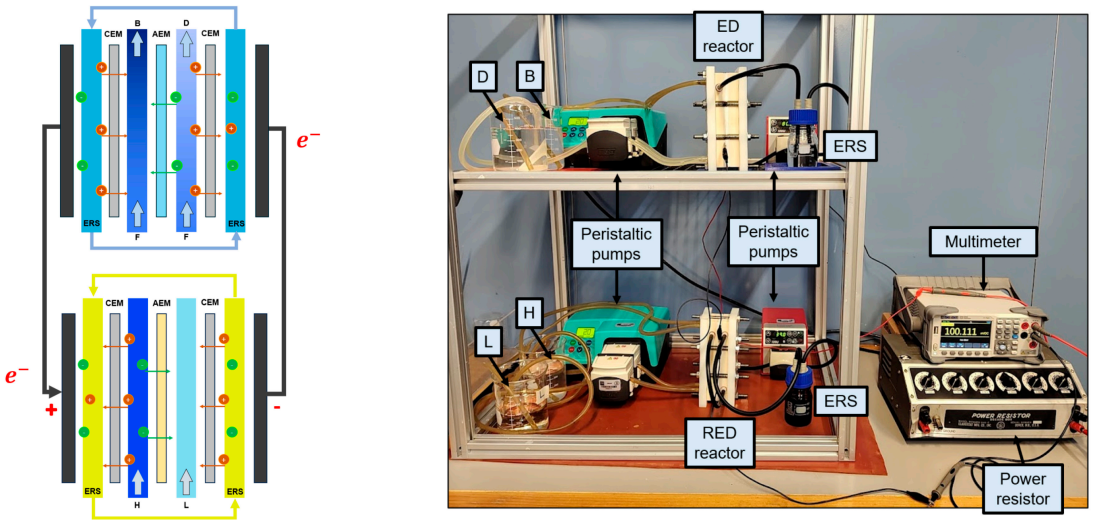

(**a**) (**b**)

Figure 9. Schematic and experimental setup of the hybrid RED-ED system: (**a**) schematic diagram of the hybrid system, showing the RED and ED reactors connected electrically but operating with independent solutions; (**b**) photograph of the experimental setup, illustrating the RED and ED reactors connected, peristaltic pumps, multimeter, and the power resistor.

The ED desalination process, powered entirely by the RED reactor, was evaluated under two different operational configurations for the RED system: continuous and batch modes. The flow rate selected for the RED reactor was 80 mL/min, based on prior studies. The ED process was conducted in batch mode at two different flow rates, 40 mL/min and 80 mL/min. Figure 10 illustrates the progression of desalination over time for the hybrid system under both experimental conditions. Figure 10a shows the performance of the system when the ED unit was operated at a flow rate of 40 mL/min. The purple lines represent the experiments with the RED reactor in batch mode, while the blue lines represent those conducted with RED in continuous mode. Figure 10b presents the results for the ED process at 80 mL/min, where the pink lines indicate batch operation of the RED reactor, and the green lines correspond to the continuous process.

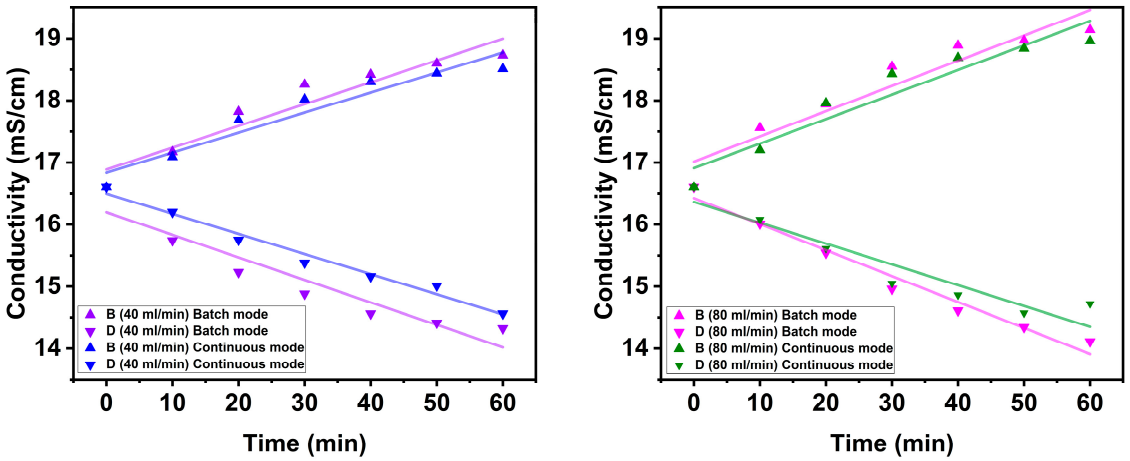

(**a**) (**b**)

Figure 10. Conductivity variation during ED desalination powered by RED under different operational modes: (**a**) conductivity behavior with ED operated at 40 mL/min under batch and continuous modes for the RED reactor; (**b**) conductivity response with ED operated at 80 mL/min under both batch and continuous RED modes.

In both sets of experiments, the batch mode exhibited superior desalination performance compared to the continuous mode, indicating that in shorter experiments, the decrease in the salinity gradient in the batch mode did not significantly impact desalination efficiency. The graphs in Figure 10 show a consistent decrease in conductivity in the desalinated compartment and an increase in the brine compartment, demonstrating effective ion transport under the energy supplied by the RED reactor. However, for longer experimental durations, it is anticipated that the reduction in the salinity gradient could negatively affect the hybrid system's performance, potentially diminishing the energy available to drive the ED process effectively. The desalination rate for each scenario was calculated as the difference between the initial and final conductivity of the desalinated water, and the results are presented in Table 5. In our study, the RED/ED system operated with an initial salt concentration of 10 g/L, achieving the highest efficiency of a 15% reduction in salt concentration within one hour at a flow rate of 80 mL/min in batch mode. This process had a specific energy consumption of 0.1388 Wh/m^3 and a recovery rate of 50%. In comparison, ref. [22] used a 50-cell RED/ED stack with initial concentrations of 30 g/L and 0.5 g/L in the high- and low-salinity compartments, respectively. Their system achieved over 90% desalination with an energy consumption of 0.004–0.065 kWh/m^3 by leveraging salinity gradients. Ref. [16] employed a PFED configuration with 20 RED cell pairs, reaching potable water standards at 72 µS/cm without external power. Similarly, ref. [15] used a hybrid RED/ED approach, achieving over 90% desalination for high-salinity wastewater. Unlike multi-cell setups, our single-cell configuration offers a simplified, effective method for moderate desalination targets, with practical energy efficiency at a 10 g/L salt concentration.

Table 5. Salt removal efficiency under different operational conditions.

ED Flow Rate (mL/min)	RED Mode	Salt Removal (%)
40	Continuous	12.28
40	Batch	13.73
80	Continuous	12.22
80	Batch	15.00

4. Discussion

This study presents a practical methodology for the development of a hybrid desalination system based on 3D-printed RED and ED reactors. The primary objective was to demonstrate the feasibility of creating a functional desalination system in a laboratory setting using accessible technologies like additive manufacturing. This work aims to bridge the gap between concept and application, offering a detailed pathway for developing electrochemical flow reactors that can be tailored for various purposes, including desalination.

The results demonstrate that the hybrid RED-ED system is functional, achieving a salt removal efficiency of 15% in one hour. While this efficiency may not be among the highest for desalination systems, it serves as a proof of concept, showing that the hybrid configuration is capable of effective operation, even at a basic level with single-unit cells. The modular design of the system also implies that its efficiency could be improved significantly by adding more unit cells, increasing the reactor size, employing profiled membranes, or reducing the distance between the membranes, all of which would enhance ion transport, reduce energy losses, and improve overall desalination performance.

An analysis of variance (ANOVA) conducted on the experimental data, detailed in Appendix A, confirmed that the observed effects were statistically significant, with p-values below 0.05, indicating that the variations were not random. This statistical robustness supports the reliability of the reactor performance under different operational conditions. Additionally, Pearson correlations showed linear relationships between key variables.

In the context of desalination technology development, this approach offers an alternative methodology by leveraging 3D printing for rapid prototyping and design iteration. Unlike conventional fabrication techniques, which can be costly and time-consuming, 3D printing allows for quick adjustments and the exploration of multiple design configurations. This adaptability not only accelerates the prototyping process but also reduces costs associated with manufacturing. Furthermore, by enabling rapid design iteration, the methodology makes it possible to optimize system configurations more efficiently, contributing to the advancement of hybrid desalination technologies.

Future research directions could involve exploring the long-term operational stability of the system, particularly comparing batch and continuous modes for the RED reactor. The short-term experiments showed that batch mode resulted in better desalination performance, but for extended durations, maintaining a consistent salinity gradient through continuous operation might prove more effective. Additionally, investigating the use of alternative, more cost-effective printing materials and optimizing membrane materials could further improve the economic viability of the system. This study highlights the potential of 3D printing for developing hybrid RED-ED desalination systems. The flexibility offered by this technology, combined with rapid prototyping capabilities, enables researchers to iterate quickly and adapt the design to specific research needs, advancing the development of hybrid systems and opening avenues for further research on scaling and optimization.

Author Contributions: Z.D.l.C.-B.: conceptualization, experimental activities, formal analysis, writing—original draft preparation. E.S.-S.: experimental activities, methodology, writing—original draft preparation. J.I.H.-H.: data curation, visualization. M.M.-H.: writing—review and editing, project administration. E.M.: writing—review and editing, project administration. All authors have read and agreed to the published version of the manuscript.

Funding: This research was funded by the PAPIIT-DGAPA-UNAM project, grant number IN112724 and by the Instituto de Ingeniería, UNAM, Grupos Interdisciplinarios de Investigación (GII), Project: "Sostenibilidad del Caribe mexicano: Cambiando debilidades en fortalezas".

Data Availability Statement: The original contributions presented in the study are included in the article, further inquiries can be directed to the corresponding authors.

Acknowledgments: Z. De la Cruz-Barragán, E. Sandoval-Sánchez, and J.I. Hernández-Hernández thank CONAHCYT for the doctoral scholarships.

Conflicts of Interest: The authors declare no conflicts of interest. The funders had no role in the design of the study; in the collection, analyses, or interpretation of data; in the writing of the manuscript; or in the decision to publish the results.

Appendix A

This appendix presents a detailed analysis of variance (ANOVA) to assess the statistical significance of variations observed across different experimental groups within the hybrid RED/ED system, comparing continuous (Co) and batch (Ba) modes. Each experimental group contains seven data points, which are averages from at least three repetitions of each experiment. This consistent sample size across all groups establishes a solid foundation for subsequent comparisons. The results of the ANOVA analysis are presented in Table A1, providing a comprehensive view of the statistical metrics calculated for each group.

The degrees of freedom (*DF*) for error within each group were calculated based on the model structure, considering the total number of observations and the parameters estimated. Specifically, the degrees of freedom in this analysis follow Equation (A1):

$$DF_{ERROR} = N - DF_{model} - 1 \quad \text{(A1)}$$

where N represents the total observations (7 points per group), and the DF model is the number of estimated parameters, excluding the intercept. This standardized approach enables a consistent and reliable estimation of error across all models, facilitating robust comparisons between the batch and continuous modes.

Pearson's correlation coefficients (r) provide insight into the linear relationships between the studied variables. The Pearson correlation coefficients (r) reveal strong linear relationships between the studied variables in both the brine and desalinated water streams. Positive correlations in the brine stream indicate a direct relationship between operational time and conductivity, where conductivity increases as time progresses. This trend is consistent in both batch and continuous modes, as shown by the upward slope in the graph. In contrast, the desalinated water stream exhibits negative correlations, reflecting an inverse relationship between time and conductivity, where conductivity decreases over time as the desalination process advances. This inverse trend highlights the system's effectiveness in reducing salinity in the desalinated stream over time. The opposing behaviors observed—where conductivity rises in the brine stream due to salt concentration and falls in the desalinated stream as ions are removed—underscore the system's efficiency in achieving ion separation, with the Pearson correlation coefficients capturing these linear relationships robustly.

The F-values reported in the ANOVA table, which represent the ratio of the variance explained by the model to the unexplained variance, underscore the robustness of the models. High F-values, paired with p-values well below the 0.05 threshold, indicate that the observed variance is largely attributed to the experimental factors rather than random variability. This statistical significance implies that the effects captured by the models are the result of genuine relationships between the variables rather than random fluctuations within the data, applicable to both batch and continuous modes. The R-squared (R^2) values further corroborate this interpretation, showing that a significant portion of the data variability is explained by the models, with values close to 1 indicating a strong fit. This robustness in model fit, combined with the consistency in sample size and degrees of freedom, reinforces the reliability of the statistical findings. The high R-squared values suggest that the models effectively capture the dynamics of the system, providing a reliable basis for understanding the interplay between operational parameters and desalination outcomes in the RED/ED hybrid system.

Table A1. ANOVA of the desalination process in the RED/ED hybrid system.

ANOVA/Var	B_40_Ba	D_40_Ba	B_40_Co	D_40_Co	B_80_Ba	D_80_Ba	B_80_Co
Number of Points	7	7	7	7	7	7	7
Degrees of Freedom	5	5	5	5	5	5	5
Residual Sum of Squares	0.330	0.406	0.245	0.061	0.470	0.135	0.431
Pearson's r	0.955	−0.949	0.960	−0.989	0.952	−0.986	0.954
R-Square (COD)	0.912	0.900	0.922	0.979	0.907	0.973	0.910
F Value	52.461	45.392	59.627	239.765	49.281	182.138	50.919
Prob > F	7.83×10^{-4}	0.001	5.82×10^{-4}	2.04×10^{-5}	9.05×10^{-4}	4.00×10^{-5}	8.39×10^{-4}

References

1. Jones, E.; Qadir, M.; van Vliet, M.T.H.; Smakhtin, V.; Kang, S.M. The state of desalination and brine production: A global outlook. *Sci. Total Environ.* **2019**, *657*, 1343–1356. [CrossRef] [PubMed]
2. Micale, G.; Cipollina, A.; Rizzuti, L. Seawater desalination for fresh water production. In *Seawater Desalination*; Springer: Berlin/Heidelberg, Germany, 2009; pp. 1–15. [CrossRef]
3. Al-Karaghouli, A.; Kazmerski, L.L. Energy consumption and water production cost of conventional and renewable-energy-powered desalination processes. *Renew. Sustain. Energy Rev.* **2013**, *24*, 343–356. [CrossRef]
4. Angelakis, A.N.; Valipour, M.; Choo, K.-H.; Ahmed, A.T.; Baba, A.; Kumar, R.; Toor, G.S.; Wang, Z. Desalination: From ancient to present and future. *Water* **2021**, *13*, 2222. [CrossRef]
5. Campione, A.; Gurreri, L.; Ciofalo, M.; Micale, G.; Tamburini, A.; Cipollina, A. Electrodialysis for water desalination: A critical assessment of recent developments on process fundamentals, models and applications. *Desalination* **2018**, *434*, 121–160. [CrossRef]
6. Ali, A.; Tufa, R.A.; Macedonio, F.; Curcio, E.; Drioli, E. Membrane technology in renewable-energy-driven desalination. *Renew. Sustain. Energy Rev.* **2018**, *81*, 1–21. [CrossRef]
7. Alkaisi, A.; Mossad, R.; Sharifian-Barforoush, A. A Review of the Water Desalination Systems Integrated with Renewable Energy. *Energy Procedia* **2017**, *110*, 268–274. [CrossRef]
8. Cipollina, A.; Micale, G. *Sustainable Energy from Salinity Gradients*; Woodhead Publishing: Sawston, UK, 2016. [CrossRef]
9. Veerman, J.; Saakes, M.; Metz, S.J.; Harmsen, G.J. Reverse electrodialysis: Evaluation of suitable electrode systems. *J. Appl. Electrochem.* **2010**, *40*, 1461–1474. [CrossRef]
10. Pattle, R.E. Production of electric power by mixing fresh and salt water in the hydroelectric pile. *Nature* **1954**, *174*, 660. [CrossRef]
11. Jia, Z.; Wang, B.; Song, S.; Fan, Y. Blue energy: Current technologies for sustainable power generation from water salinity gradient. *Renew. Sustain. Energy Rev.* **2014**, *31*, 91–100. [CrossRef]
12. Mermier, N.R.J.D.; Borges, C.P. Direct osmosis process for power generation using salinity gradient: FO/PRO pilot plant investigation using hollow fiber modules. *Chem. Eng. Process. Process Intensif.* **2016**, *103*, 27–36. [CrossRef]
13. Post, J.W. Blue Energy: Electricity Production from Salinity Gradients by Reverse Electrodialysis. Ph.D. Thesis, Wageningen University, Wageningen, The Netherlands, 2009.
14. Vermaas, D.A. Energy Generation from Mixing Salt Water and Fresh Water. Ph.D. Thesis, University of Twente, Enschede, The Netherlands, 2014. [CrossRef]
15. Wang, Q.; Gao, X.; Zhang, Y.; He, Z.; Ji, Z.; Wang, X.; Gao, C. Hybrid RED/ED system: Simultaneous osmotic energy recovery and desalination of high-salinity wastewater. *Desalination* **2017**, *405*, 59–67. [CrossRef]
16. Luo, F.; Wang, Y.; Jiang, C.; Wu, B.; Feng, H.; Xu, T. A power free electrodialysis (PFED) for desalination. *Desalination* **2017**, *404*, 138–146. [CrossRef]
17. Chen, Q.; Liu, Y.Y.; Xue, C.; Yang, Y.L.; Zhang, W.M. Energy self-sufficient desalination stack as a potential fresh water supply on small islands. *Desalination* **2015**, *359*, 52–58. [CrossRef]
18. Chen, M.; Mei, Y.; Yu, Y.; Zeng, R.J.; Zhang, F.; Zhou, S.; Tang, C.Y. An internal-integrated RED/ED system for energy-saving seawater desalination: A model study. *Energy* **2019**, *170*, 139–148. [CrossRef]
19. Ambrosi, A.; Shi, R.R.S.; Webster, R.D. 3D-printing for electrolytic processes and electrochemical flow systems. *J. Mater. Chem. A Mater.* **2020**, *8*, 21902–21929. [CrossRef]
20. O'Connor, H.; Bailey, J.J.; Istrate, O.M.; Klusener, P.A.A.; Watson, R.; Glover, S.; Iacoviello, F.; Brett, D.J.L.; Shearing, P.R.; Nockemann, P. An open-source platform for 3D-printed redox flow battery test cells. *Sustain. Energy Fuels* **2022**, *6*, 1529–1540. [CrossRef]
21. Bai, X.; Sano, Y.; Amagai, S.; Nakayama, A. An experimental study on the performance of an electro-dialysis desalination using hollow cubic assembled porous spacers fabricated by a 3D printer. *Desalination* **2018**, *445*, 6–14. [CrossRef]
22. Chen, C.; Jiang, J.; He, W.; Lei, W.; Hao, Q.; Zhang, X. 3D Printed High-Loading Lithium-Sulfur Battery Toward Wearable Energy Storage. *Adv. Funct. Mater.* **2020**, *30*, 1909469. [CrossRef]
23. Manzanares-Palenzuela, C.L.; Hermanova, S.; Sofer, Z.; Pumera, M. Proteinase-sculptured 3D-printed graphene/polylactic acid electrodes as potential biosensing platforms: Towards enzymatic modeling of 3D-printed structures. *Nanoscale* **2019**, *11*, 12124–12131. [CrossRef]
24. Arenas, L.F.; Ponce de León, C.; Walsh, F.C. 3D-printed porous electrodes for advanced electrochemical flow reactors: A Ni/stainless steel electrode and its mass transport characteristics. *Electrochem. Commun.* **2017**, *77*, 133–137. [CrossRef]

25. Cardoso, R.M.; Kalinke, C.; Rocha, R.G.; dos Santos, P.L.; Rocha, D.P.; Oliveira, P.R.; Janegitz, B.C.; Bonacin, J.A.; Richter, E.M.; Munoz, R.A. Additive-manufactured (3D-printed) electrochemical sensors: A critical review. *Anal. Chim. Acta* **2020**, *1118*, 73–91. [CrossRef] [PubMed]
26. Gonzalez-Vogel, A.; Felis-Carrasco, F.; Rojas, O.J. 3D printed manifolds for improved flow management in electrodialysis operation for desalination. *Desalination* **2021**, *505*, 114996. [CrossRef]
27. Cervantes-Alcalá, R.; Miranda-Hernández, M. Flow distribution and mass transport analysis in cell geometries for redox flow batteries through computational fluid dynamics. *J. Appl. Electrochem.* **2018**, *48*, 1243–1254. [CrossRef]
28. Cruz-Díaz, M.R.; Laureano, A.; Rodríguez, F.A.; Arenas, L.F.; Pijpers, J.J.H.; Rivero, E.P. Modelling of flow distribution within spacer-filled channels fed by dividing manifolds as found in stacks for membrane-based technologies. *Chem. Eng. J.* **2021**, *423*, 130232. [CrossRef]
29. Gurreri, L.; Tamburini, A.; Cipollina, A.; Micale, G.; Ciofalo, M. CFD prediction of concentration polarization phenomena in spacer-filled channels for reverse electrodialysis. *J. Membr. Sci.* **2014**, *468*, 133–148. [CrossRef]
30. Gurreri, L.; Tamburini, A.; Cipollina, A.; Micale, G.; Ciofalo, M. Flow and mass transfer in spacer-filled channels for reverse electrodialysis: A CFD parametrical study. *J. Membr. Sci.* **2016**, *497*, 300–317. [CrossRef]
31. Rivera, F.F.; Pérez, T.; Castañeda, L.F.; Nava, J.L. Mathematical modeling and simulation of electrochemical reactors: A critical review. *Chem. Eng. Sci.* **2021**, *239*, 116622. [CrossRef]
32. Patel, S.K.; Qin, M.; Walker, W.S.; Elimelech, M. Energy Efficiency of Electro-Driven Brackish Water Desalination: Electrodialysis Significantly Outperforms Membrane Capacitive Deionization. *Environ. Sci. Technol.* **2020**, *54*, 3663–3677. [CrossRef]
33. Xu, X.; He, Q.; Ma, G.; Wang, H.; Nirmalakhandan, N.; Xu, P. Selective separation of mono- and di-valent cations in electrodialysis during brackish water desalination: Bench and pilot-scale studies. *Desalination* **2018**, *428*, 146–160. [CrossRef]
34. Levenspiel, O. Tracer Technology: Modeling the Flow of Fluids. 2011. Available online: http://www.springer.com/series/5980 (accessed on 15 June 2024).
35. Bengoa, C.; Montillet, A.; Legentilhomme, P.; Legrand, J. Flow visualization and modelling of a Filter-press type electrochemical reactor. *J. Appl. Electrochem.* **1997**, *27*, 1313–1322. [CrossRef]